Displacement and burial mechanisms of objects by granular flows: towards implications for post-disaster search and rescue

Ji, W.[1], Fang, J.*[1], Zhao, J.[2], Wang, Y.[2], Xue, T.[2], and Choi, C.E.*[1]

[1] Department of Civil Engineering, The University of Hong Kong

[2] Department of Civil and Environmental Engineering, The Hong Kong University of Science and Technology

*Co-corresponding authors: cechoi@hku.hk and junfan@hku.hk

Abstract

Flow-type landslides can displace and bury structures in hazard-prone areas. Such events create vast and poorly defined search zones that make rescue efforts challenging, especially if they must be completed within a critical 72-hour survival window. This study leverages a high fidelity multi-scale solver (coupled Material Point Method and Spheropolyhedron Discrete Element Method) to reveal the fundamental mechanisms of the displacement and transport of objects by granular flows. A parametric analysis is carried out to investigate the effects of flow velocity and depth, block density, basal friction, initial orientation, and block aspect ratio on the block displacement and transport based on entirely and partially submerged modes. A dimensionless number, the impact Froude number, is demonstrated to reliably predict the normalized travel distances of blocks for both modes. Travel distances inversely correlate with basal friction and block-to-flow density ratio, driven by frictional dissipation during deceleration. Orthogonal impacts maximize distances due to sustained momentum, increasing search challenges for perpendicular structures. Low-aspect-ratio blocks travel farther than slender ones owing to less overturning and velocity loss. A contour chart maps runout against Froude number, friction, and density, exposing high sensitivity in submerged regimes and serving as a practical guiding tool to enhance search and rescue operations.

Keywords: flow-type landslide, block transport, recovery, impact, disaster response, MPM-SDEM

1. Introduction

Flow-type landslides, including rock and snow avalanches, are common geological hazards in mountainous regions worldwide (Iverson, 1997; Cuomo, 2020; Mani et al., 2023). One of the most significant hazard scenarios is when they displace and bury objects with victims trapped inside (Collins et al., 2003). Displaced objects from their original locations make rescue efforts considerably more challenging. A notable example is the 2006 Guinsaugon event, where rescuers wasted the first six days digging in the wrong location because the entire village was displaced 600 m downslope (Lagmay et al., 2008). In addition, it is documented that in the 2015 Longyearbyen snow avalanche, 11 houses were displaced and buried, resulting in failed efforts to recover the victims without clear search areas to focus on (Indreiten and Svarstad, 2016). Thus, a comprehensive investigation of how these events transport and bury objects is essential to guide and advance search and rescue efforts.

The transport and burial mechanisms of objects in flow-type landslides can be closely attributed to the high mobility and dynamic impact by these events. Extensive research, incorporating field observations, laboratory experiments, and numerical simulations, has focused on the interactions between such landslides and objects such as rigid barriers and walls (Schuster, 2006; Sovilla et al., 2012; Thouret et al., 2020). These studies indicate that dynamic impact of the landslide is strongly controlled by its flow composition, including grain size and solid concentration (Hungr et al., 2001; Iverson, 1997; Thouret et al., 2020). To predict the impact force on objects, hydrostatic, hydrodynamic and hybrid impact models have been developed, which can further express the impact force as a function of the Froude number for the landslides (Ng et al., 2021).

Although significant progress has been made in elucidating the dynamics of flow impacts on objects under various conditions, existing research has primarily addressed two aspects: (1)

interactions with immobile objects such as rigid barriers and walls (Ceccato et al., 2018; Ng et al., 2021; Yu et al., 2025), and (2) predicting the initiation of motion for mobile objects (Liu et al., 2025; Luo et al., 2025). In contrast, the full transport and burial processes of mobile non-spherical objects, including their complete spatiotemporal trajectories, velocity evolution, energy transfer mechanisms, and final burial locations, remain poorly understood. This knowledge gap exists because interactions between flow-type landslides and mobile objects are considerably more complex than those involving fixed obstacles. Additional factors such as basal friction, buoyancy, and drag forces must be accounted for to accurately capture transport and burial mechanisms. Furthermore, a detailed spatiotemporal analysis of object motions (e.g., rolling, sliding, and bouncing) is essential to provide meaningful guidance for post-disaster search and rescue operations. Currently, there is a notable lack of physical evidence and fundamental insights into the interaction mechanisms between flow-type landslides and mobile objects. As a result, existing empirical models are largely limited to predicting the initiation of object motion (Luo et al., 2025), rather than capturing their full spatiotemporal trajectories. Feng and Song (2025) studied the complicated physical mechanisms associated with the movement of building fragments, demonstrating that the Froude number is a key parameter governing the travel distance of blocks in the flow. Nevertheless, the Froude number primarily accounts for the flow mobility, failing to incorporate the inertia of building fragments. More studies are still required.

Lab-scale laboratory experiments are a cost-effective and widely adopted approach. However, the inherent opacity of dense, high-mobility granular or two-phase flows severely restricts direct visual observation and real-time tracking of object motion within the flow (Sun et al., 2024; Escobar et al., 2025). This fundamental limitation renders conventional physical experiments inadequate for resolving the detailed interaction mechanics of mobile objects such as buildings. Alternatively, various numerical approaches have been developed to simulate the landslides impacting objects, including continuum models (Liu et al., 2024), discrete methods (Salciarini et al., 2010), and hybrid approaches (Trujillo-Vela et al., 2020; Ren et al., 2022). Discrete methods are prohibitively expensive due to the need to track every particle explicitly (Zhao et al., 2023), while continuum methods struggle to accurately capture the rotational motion and momentum exchange of objects (Liu et al., 2018; Jiang et al., 2020). Fang et al. (2026) developed an efficient hybrid method, a coupled framework of Material Point Method and spheropolyhedron Discrete Element Method (MPM-SDEM), to balance accuracy and efficiency by solving flow-type landslides and objects using MPM and SDEM, respectively. It should be noted that objects in real-world application typically have non-spherical shapes. The SDEM offers particular advantages for faithfully reproducing the geometry and contact behavior of real-world objects such as buildings, vehicles, or boulders (Jiang et al., 2020; Ren et al., 2025). This coupled MPM-SDEM framework has been demonstrated to reliably simulate the complex entrainment, transport, and burial of objects in high-mobility landslides (Fang et al., 2026).

In this study, we use a well-calibrated MPM-SDEM solver (Fang et al., 2026) to elucidate the transport and burial mechanisms of movable non-spherical objects in flow-type landslides. Through comprehensive parametric studies and systematic dimensionless analysis, we identify the dominant governing parameters and establish a reliable predictive relationship between the impact Froude number and normalized travel distance. We further quantify how basal friction, density ratio, initial orientation, and aspect ratio affect block displacement, providing mechanistic insights that were previously unavailable. Finally, we synthesize these findings into practical contour charts that integrate impact Froude number, basal friction, and density ratio. These charts serve as a rapid, field-applicable tool for estimating probable displacement zones, directly supporting more efficient post-disaster search and rescue operations, which is an outcome that fixed-object impact models cannot provide.

2. Methodology

2.1 Computational modeling of flow-block interactions

In particular, the SDEM component enables accurate rigid-body rotation through quaternion-based kinematics, which preserves angular momentum conservation and avoids the numerical instabilities or artificial damping commonly encountered in continuum-based rigid body treatments within pure MPM frameworks (Fang et al., 2026). Furthermore, by representing non-spherical objects as sphero-polyhedra, the method transforms singular sharp-corner contacts into smooth, continuous primitive interactions (vertex-face, edge-edge, and vertex-edge). This provides robust handling of complex multi-point contacts with significantly reduced force oscillations and numerical noise, which is essential for realistically capturing the progressive overturning and full transport trajectories of mobile blocks(Jiang et al., 2020). In direct comparison with MPM-LSDEM, MPM-SDEM improves computational efficiency by up to 97% while enhancing accuracy in predicting block travel distance by up to 63%)(Fang et al., 2026). These features are particularly advantageous for mobile objects, whose motion involves rotation, overturning, and sustained multi-contact interactions that are absent in fixed-object impact problems.

2.1.1 Discrete modeling of non-spherical particle

The SDEM models non-spherical, rigid particles as a spheropolyhedron, formed by the Minkowski sum of a core polyhedron and a sphere. This creates a non-spherical particle with rounded edges and corners while preserving the original geometry, including face, edge and vertex. This approach can eliminate sharp-edge singularities, which reduces contact multiplicity, and improves numerical stability and efficiency. The translational and rotational motions of SDEM particle are solved by Newton's second law, which can be written as:

$$m_{\mathrm{Pi}}\frac{d\,\boldsymbol{v}_{\mathrm{Pi}}}{d\,t} = \sum_{j=1}^{n_{\mathrm{i}}} \boldsymbol{F}_{\mathrm{ij}} + \boldsymbol{F}_{\mathrm{g}} + \sum_{p=1}^{n_{\mathrm{p}}} \boldsymbol{F}_{\mathrm{c,p}}, \tag{1}$$

$$I_{\mathrm{Pi}}\frac{d\,\boldsymbol{w}_{\mathrm{Pi}}}{d\,t} = \sum_{j=1}^{n_{\mathrm{i}}} \boldsymbol{M}_{\mathrm{ij}} + \sum_{p=1}^{n_{\mathrm{p}}} \boldsymbol{M}_{\mathrm{c,p}}, \tag{2}$$

Here, m_{pi} and I_{pi} denote the mass and moment of inertia of an individual SDEM particle i. Meanwhile, $\boldsymbol{v}_{\mathrm{Pi}}$ and $\boldsymbol{w}_{\mathrm{Pi}}$ represent the linear and angular velocities of particle i, respectively. n_{i} indicates the contact number between particle i and other SDEM particles. n_{p} is the contact number between particle i and material points (MPs). $\boldsymbol{F}_{\mathrm{c,p}}$ and $\boldsymbol{M}_{\mathrm{c,p}}$correspond to the contact forces and moments exerted on particle i from MPs, respectively. $\boldsymbol{F}_{\mathrm{ij}}$ and $\boldsymbol{M}_{\mathrm{ij}}$ are the contact force and torque applied to particle i by SDEM particle j. $\boldsymbol{F}_{\mathrm{g}}$ is the gravitational force.

2.1.2 Continuum modeling of flow-type landslide

Previous researches (Cui et al., 2021; Dunatunga & Kamrin, 2015) have demonstrated that continuum frameworks can effectively model the flow event. These frameworks can describe three distinct rheological regimes: elastic, plastic, and gasified (Liang et al., 2023). In this study, the elastic response is formulated using Hencky elasticity to account for finite deformation and geometric nonlinearity. The plastic regime is governed by the Drucker-Prager yield criterion (Drucker & Prager, 1952). Finally, the gasified regime, characterized by intergranular detachment due to volumetric dilation, is described using a trans-phase constitutive model (Dunatunga & Kamrin, 2015, 2017), which has been rigorously validated in various scenarios involving flow-intrusion interactions (Agarwal et al., 2021; Dunatunga & Kamrin, 2017).

To solve the governing continuum equations, MPM is employed here, which is a hybrid Lagrangian-Eulerian technique for materials undergoing extensive deformation and exhibiting history-dependent constitutive behavior. The MPM can simulate both the shear-induced failure due to particle interactions and the granular gasification described by the trans-phase model (Dunatunga & Kamrin, 2015). This study utilizes a hybrid continuum-discrete numerical framework, which explicitly accounts for the discrete characteristics of coarse-grained flows. This methodology is distinct from conventional friction-based approaches that presuppose persistent flow-substrate contact.

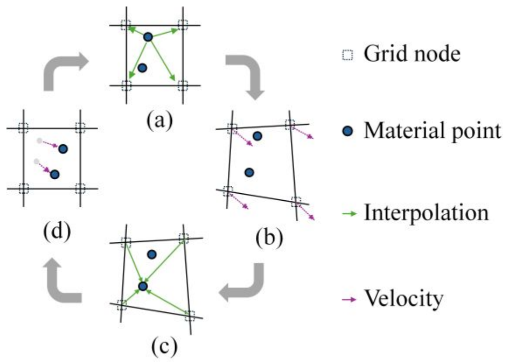

Figure 1**.** Main steps of the MPM; (a) particle-to-grid mapping (P2G); (b) grid-to-grid mapping (G2G); (c) grid-to-particle mapping (G2P); (d) particle-to-particle mapping (P2P)

The MPM algorithm comprises four principal phases, as illustrated in Figure 1. The process initiates with the particle-to-grid (P2G) mapping (Figure 1a), where the mass and momentum of the Lagrangian material points are projected onto the nodes of the background Eulerian mesh. This study utilizes the generalized interpolation material point method (GIMP), which mitigates cell-crossing instabilities and shows robust performance in scenarios involving particle separation (Fei et al., 2021). In the subsequent phase (Figure 1b), the nodal momenta are updated in accordance with the discretized momentum balance equations. The momentum conservation is as follows:

$$\rho \frac{D\boldsymbol{v}}{Dt} = \nabla \cdot \boldsymbol{\sigma} + \rho \boldsymbol{b} + \boldsymbol{f}_{\mathrm{c}} \tag{3}$$

where ρ is the bulk density, t is time, $\boldsymbol{\sigma}$ is the Cauchy stress tensor, and $\boldsymbol{b}$ represents the acceleration resulting from the coupling forces caused by the flow-block interactions (to be discussed) and the gravity. $\boldsymbol{f}_{\mathrm{c}}$ is the volume-averaged force density, which is derived from contact forces between MPM and SDEM.

The algorithm then proceeds to the third stage (Figure 1c), the grid-to-particle mapping. During this phase, the updated nodal quantities (such as velocity and acceleration) are interpolated back to the material points. This study employs a hybrid G2P transfer that blends the Fluid-Implicit-Point method with the Particle-in-Cell method (Liang et al., 2023). This blended approach is strategically chosen to balance the competing demands of numerical stability and energy conservation. Finally, the fourth stage (Figure 1d) updates the MP properties (e.g., position) and advances the simulation to the next time step.

2.1.3 Coupling between flow-type landslide and non-spherical particles

In the MPM-SDEM algorithm, each MP is assigned an equivalent spherical radius, which is derived from its volume to ensure strict volumetric consistency with the continuum representation. Then the MP sphere is detected and determined whether the overlap with the surface elements (faces, edges, or vertices) of the SDEM particles is established. If so, the coupling force $\boldsymbol{F}_{\mathrm{c,p}}$ between the MP and the SDEM particle is calculated, where the normal elastic force $\boldsymbol{F}_{\mathrm{ij}}^{\mathrm{n}}$ is calculated based on Hooke's law), and the shear force $\boldsymbol{F}_{\mathrm{ij}}^{\mathrm{s}}$ is determined based on Coulomb friction law (Ren et al., 2022), as following:

$$\boldsymbol{F}_{\mathrm{ij}}^{\mathrm{n}} = K_{\mathrm{n}}\,\delta, \tag{4}$$

$$\boldsymbol{F}_{\mathrm{ij}}^{\mathrm{s}} = \min\{\mu\,\boldsymbol{F}_{\mathrm{ij}}^{\mathrm{n}}, -\,K_{\mathrm{t}}\xi - c_{\mathrm{t}}v_{\mathrm{t}}\}, \tag{5}$$

where δ is overlapping distance between MP and SDEM particle, ξ is the cumulative tangential displacement before sliding occurs, and μ is the frictional coefficient. v_{t} is the tangential relative velocity, c_{t} is the damping coefficient. K_{n} is the normal contact stiffness, and K_{t} is tangential contact stiffness, respectively, expressed by the equation (Zhao et al., 2022; Liu et al., 2018b) as following:

$$K_{\mathrm{n}} = -k_{\mathrm{c}}\delta\left[2\ln\left(\frac{R-\delta}{R}\right) - \frac{R}{R-\delta} + 1\right], \tag{6}$$

$$K_{\mathrm{t}} = K_{\mathrm{n}}/2(1+\upsilon), \tag{7}$$

where k_{c} is barrier stiffness parameter (Zhao et al., 2022). υ is Poisson's ratio. The sum of $\boldsymbol{F}_{\mathrm{ij}}^{\mathrm{n}}$ and $\boldsymbol{F}_{\mathrm{ij}}^{\mathrm{s}}$ on MP is then mapped to adjacent background nodes as part of the external force, as $\boldsymbol{f}_{\mathrm{c}}$ in Eq. (3).

2.2 Fundamentals of dimensional analysis

Having established the coupled MPM-SDEM framework for simulating flow-block interactions, it is necessary to scale the numerical model from prototype conditions to a computationally feasible small-scale model while preserving dynamic similarity(Iverson, 2015). The adoption of a small-scale model also enables systematic parametric studies across a wide range of flow conditions, block properties, and geometric configurations within reasonable computational time, which would be infeasible at full prototype scale. This approach is consistent with established practices in both physical flume experiments and numerical modelling of debris flows and landslides (Iverson, 2015; Feng & Owen, 2014).

2.2.1 Scaling law to small-scale numerical model

A geometric scale factor β = 40 is adopted in this study, which falls into the geometric scale ratio ranging from 20 to 100 (Iverson, 2015; Choi et al., 2017), to downscale prototype conditions to laboratory-derived model parameters. This scaling adheres strictly to Froude similarity criteria, with density and gravitational acceleration scales maintained at unity, velocity scaling as $\sqrt{\beta}$, and bulk modulus scaling linearly with β to preserve Cauchy number similitude. The selected β yields prototype parameters that align closely with observed mid-scale events, such as those affecting residential areas or infrastructure on alluvial fans, as documented in field and numerical studies.

This study aims to clarify how a cube-shaped block slides in an inclined flume driven by a flow-type landslide. The travel distance of the block, called S_{b}, which means the distance between initial block position and final block position along the flow direction, depends on several parameters: flow velocity v_{f}, flow depth h_{f}, block height h_{b}, flow density ρ_{f}, block density ρ_{b}, gravity g, friction coefficient between block and flume bed μ_{b}, slope angle θ, initial orientation φ (the angle between the upstream face of the block and the flow direction) and aspect ratio As_{b} of the block. The scale factors for key variables are summarised in

Table 1.

Table 1. Scale factors for the relevant variables considered in the model impact tests, following the density-length-acceleration principle.

Parameter	Variables	Prototype Range	Model Range	Scaling Ratio
Gravity	g	9.81 m/s²	9.81 m/s²	β_g=1
Flow density	ρ_f	1600 kg/m³	1600 kg/m³	β_ρ=1
Block density	ρ_b	1600 ~ 8900 kg/m³	1600 ~ 8900 kg/m³	β_ρ=1
Flow depth	h_f	1.24 ~ 5.00 m	0.031 ~ 0.125 m	$\beta_h = \beta = 40$
Block height	h_b	2.00 m	0.05 m	$\beta_h = \beta = 40$
Flow velocity	v_f	6.96 ~ 27.76 m/s	1.10 ~ 4.39 m/s	$\beta_v = \sqrt{\beta} \approx 6.32$
Flow bulk modulus	E	40 MPa	1 MPa	$\beta_E = \beta = 40$
Froude number	Fr	1.04 ~ 11.82	1.04 ~ 11.82	1
Basal friction coefficient of block	μ_b	0.3 ~ 1.5	0.3 ~ 1.5	1
Block aspect ratio	As_b	1.0 ~ 4.0	1.0 ~ 4.0	1
Block orientation	φ	0°~ 45°	0°~ 45°	1
Channel slope	θ	10°	10°	1

The prototype flow depth ranges from 1.24 to 5.00 m (corresponding to flow depth of 0.031-0.125 m in small-scale models), encompassing typical surge heights in channelized flow-type landslides (typically 1 - 5 m, Hübl et al., 2009; De Haas et al., 2015). Prototype front velocities span 6.96 to 27.76 m/s (scaled from model velocities of 1.10 - 4.39 m/s) (Hürlimann et al., 2003; Hübl et al., 2009; De Haas et al., 2015), consistent with measured velocities in natural flow. The Froude number remains dimensionless and invariant at 1.04 - 11.82 across scales (Hübl et al., 2009), capturing the transition from subcritical to supercritical regimes. Block height in the prototype is 2.00 m (upscaled from the 0.05 m model block) (Luo et al., 2019), representative of low-rise structures or masonry buildings vulnerable to burial in hazard-prone regions. In field cases of landslides impacting structures, buildings and shelters are predominantly rectangular or cubic in morphology (Lagmay et al., 2008; Salcedo, 2000; Zhao et al., 2020), which justifies the present focus on this common geometry in the dimensionless analysis. Density ratio (block to flow) is set between 1.0 and 5.6 in both model and prototype, spanning lightweight timber/masonry to reinforced concrete relative to saturated granular slurries (Doran & Cather, 2013). Basal friction coefficient ranges invariantly from 0.3 to 1.5 (Engineering ToolBox, 2025), simulating interfaces from smooth concrete to rough natural terrain. Block aspect ratio varies from 1.0 to 4.0, covering a wide building morphologies that governing overturn of block (Feng, 2024). Orientation angles of 0° ~ 45° are examined. Channel slope is fixed at 10° in both model and prototype (Legislative Council of HKSAR, 2008), typical of deposition zones on alluvial fans. Finally, bulk modulus scales to 40 MPa in the prototype (from 1 MPa in the model), reflecting effective stiffness in dense granular continua under dynamic loading (Dunatunga and Kamrin, 2015). The numerical relationship between the model and the prototype is summarised in

Table 1.

2.2.2 Dimensionless analysis for simulation plan

The travel distance of the block is governed by multiple physical mechanisms, including flow inertia, gravitational resistance of the block, geometric effects, and frictional dissipation. To identify the key controlling dimensionless parameters, we first establish the complete functional relationship based on the relevant variables:

$$S_{\mathrm{b}} = f_1 \ (v_{\mathrm{f}},\ h_{\mathrm{f}},\ h_{\mathrm{b}},\ \rho_{\mathrm{f}},\ \rho_{\mathrm{b}}, g, \theta, \mu_{\mathrm{b}}, As_{\mathrm{b}}, \varphi) \ , \tag{8}$$

where f_1 is an unknown function.

By dimensional analysis, guided by Buckingham's π theorem (Buckingham E., 1914), there are 11 variables involving 3 fundamental dimensions (M, L, T). Therefore, the problem can be reduced to 8 independent dimensionless groups. ρ_{f}, v_{f} and h_{b} as repeating variables are selected because they are dimensionally independent and physically meaningful: ρ_{f} provides the mass scale, g provides the inertial effect, and h_{b} provides the geometric scale relevant to both block resistance and submersion. Forming the dimensionless groups systematically yields:

$$\frac{S_{\mathrm{b}}}{h_{\mathrm{b}}} = f_2\left(\frac{v_{\mathrm{f}}}{\sqrt{(gh_{\mathrm{b}})}}, \frac{h_{\mathrm{f}}}{h_{\mathrm{b}}}, \frac{\rho_{\mathrm{b}}}{\rho_{\mathrm{f}}}, \theta, \mu_{\mathrm{b}}, As_{\mathrm{b}}, \varphi\right) \tag{9}$$

where f_2 is a new unknown function. $\frac{v_{\mathrm{f}}}{\sqrt{(gh_{\mathrm{b}})}}$ is the impact Froude number Fr_{b}, which can be calculated as the product of $v_{\mathrm{f}}/\sqrt{gh_{\mathrm{f}}}$ and $h_{\mathrm{f}}/h_{\mathrm{b}}$, as follows:

$$\frac{v_{\mathrm{f}}}{\sqrt{(gh_{\mathrm{b}})}} = Fr * \sqrt{\frac{h_{\mathrm{f}}}{h_{\mathrm{b}}}} \tag{10}$$

The impact Froude number, Fr_{b}, is the ratio of the inertial force of the flow before impact to the block potential, which is the gravitational force that the flow needs to overcome to climb over the block (Ng et al., 2021). $v_{\mathrm{f}}/\sqrt{gh_{\mathrm{f}}}$ is Froude number Fr, which characterizes the ratio of inertial force and gravitational force (Mayer et al., 2017). θ is slope angle. In debris fans, slopes are typically smaller than $11°$ (Legislative Council of HKSAR, 2008). $\theta = 10°$ is used in this study. These groups make it feasible to scale things up or down (Iverson et al., 2015). The remaining groups also carry clear physical meanings: $\frac{h_{\mathrm{f}}}{h_{\mathrm{b}}}$ distinguishes entirely submerged versus partially submerged transport modes; $\frac{\rho_{\mathrm{b}}}{\rho_{\mathrm{f}}}$ measures the inertial contrast between block and flow; μ_{b}

controls frictional energy dissipation during deceleration; and As_{b} and φ capture geometric effects on stability and impulse duration.

The material properties (i.e., flow density ρ_{f}, gravity g,) of the flow-type landslides and blocks were fixed and consistent with those used in Table 1. And the block height is 50 mm. The block density ratio $\rho_{\mathrm{b}}/\rho_{\mathrm{f}}$, bed friction coefficient μ, block orientation angle φ, block aspect ratio As_{b}, flow depth h_{f}, and flow velocity v_{f} were varied. The h_{f} and v_{f} were adjusted by varying the initial column height of granular materials in the storage container and the initial distance between the block and the gate (c.f., Figure 2), as the flow depth and flow velocity evolve along the flow path. The column heights H_{i} of granular materials in the container were set to 0.4 m, 0.6 m, 0.9 m, and 1.2 m to obtain different flow velocity and flow depth. The initial distance L_0 from the block centre to the gate was varied from 0.2 m to 3.7 m.

2.3 Numerical setup and procedures

The numerical setup is shown in **Error! Reference source not found.**. The flume has a dimension with length, width and height of 15 m, 0.2 m and 0.5 m, respectively. The granular material is initialized by uniformly distributing MP within the storage container, forming a rectangular deposition. To ensure numerical stability and prevent spurious oscillations upon the sudden application of gravity force, a gravitational ramping phase is implemented during the first 0.1 s of each simulation. During this phase, the magnitude of gravitational acceleration is progressively and linearly increased from 0 to 9.81 m/s². The grid size is 10 mm, and 8 MPs are uniformly distributed in each grid. Then flow is triggered by instantaneously removing gate. All calibrated parameters are shown in Table 2, and the calibration results are shown in Appendix A. And the robustness of the numerical model is shown in Appendix B.

Before the impact tests, the free-flow tests without the block were conducted to calibrate the depth-averaging frontal flow velocity v_f and flow depths h_f (Choi et al., 2017), which serve to evaluate the flow properties reaching the block. This approach ensures precise characterization of the incident flow parameters prior to interaction. A flow depth h_f exceeding the block height h_b denotes entirely submerged mode. Conversely, when $h_\mathrm{f} < h_\mathrm{b}$, the block experiences partially submerged mode, resulting in localized impact and potential differential loading (Chehade et al., 2021).

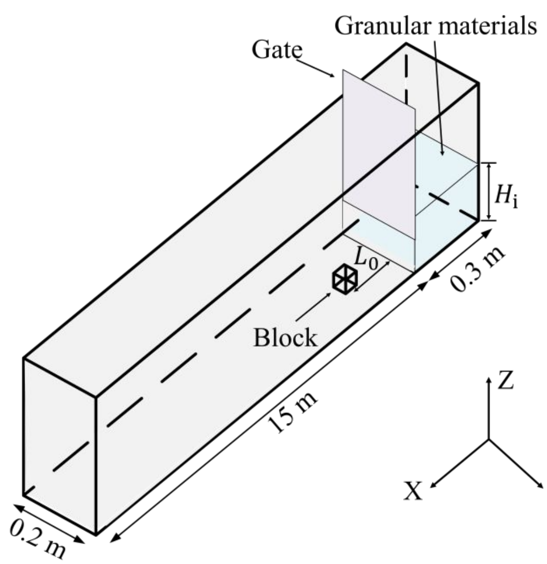

Figure 2. Numerical setup for flow-type landslide impacting a block. H_i is the initial height of granular material. L_0 is the initial distance of block away from the gate.

For the convenience of discussion, test IDs are assigned to different cases: 'PS' and 'ES' indicate the partially submerged mode and entirely submerged mode of block. 'P' indicates impact Froude number Fr_b. 'MU' is the basal frictional coefficient of block. 'RHO' is the block-to-flow density ratio. 'PHI' is the initial orientation of block. '$w_\mathrm{b}/l_\mathrm{b}$' or '$h_\mathrm{b}/l_\mathrm{b}$' means the aspect ratio of block, where $w_\mathrm{b}/l_\mathrm{b}$ specifies the ratio of block width (Y-axis) to block length (X-axis), and $h_\mathrm{b}/l_\mathrm{b}$ specifies the ratio of block height (Z-axis) to block length (X-axis). Specifically, throughout the entire simulation plan, l_b is held constant at 0.05 m. For example, when $w_\mathrm{b}/l_\mathrm{b}$ = 2, the block length (X-axis) is 0.05 m, the height (Z-axis) is 0.05 m, and the width (Y-axis) is 0.10 m. Similarly, when h_b/l_b = 3, the block length (X-axis) is 0.05 m, the height (Z-axis) is 0.15 m, and the width (Y-axis) is 0.05 m. A summary of the simulations and computed parameters are given in Table 3. A total of 67 simulations were performed.

Table 2 Summary of input parameters for calibrating the MPM-SDEM simulator.

Parameters	**Input value**	**Notes**
Density of MP	1600 kg/m^3	Measured
Young's modulus of MP	1 MPa	Liang et al., 2023
Poisson ratio of MP	0.3	Liang et al., 2023
Blending ratio of MP	0.99	Stomakhin et al., 2013
Internal friction angle of MP	13.5°	Measured
Maximum internal friction coefficient of MP	0.65	Calibrated
Density of the block	8900 kg/m^3	Measured
Radius of SDEM sphere	0.0025 m	Calibrated
Friction coefficient between block and channel	0.67	Measured
Friction coefficient between MP and channel	0.21	Calibrated
Barrier stiffness	10000 N/m	Jiang et al., 2022

Table 3 Numerical simulation plan.

Test ID	Submerged mode	Fr	v_f (m/s)	h_f/h_b	Fr_b	μ_b	ρ_b/ρ_f	θ (°)	φ (°)	As_b
ESP1.56	ES	1.04	1.1	2.31	1.56	0.67	5.6	10	0	1
ESP1.88	ES	1.62	1.32	1.37	1.88	0.67	5.6	10	0	1
PSP2.17	PS	2.50	1.52	0.77	2.17	0.67	5.6	10	0	1
PSP2.33	PS	2.94	1.63	0.64	2.33	0.67	5.6	10	0	1
PSP2.47	PS	3.43	1.73	0.52	2.47	0.67	5.6	10	0	1
ESP1.82	ES	1.23	1.27	2.21	1.82	0.67	5.6	10	0	1
ESP2.13	ES	1.90	1.49	1.27	2.13	0.67	5.6	10	0	1
PSP3.12	PS	4.17	2.19	0.57	3.12	0.67	5.6	10	0	1
PSP3.53	PS	5.31	2.47	0.45	3.53	0.67	5.6	10	0	1
PSP4.09	PS	7.09	2.86	0.34	4.09	0.67	5.6	10	0	1
ESP2.06	ES	1.45	1.44	2.05	2.06	0.67	5.6	10	0	1
ESP2.57	ES	2.16	1.8	1.44	2.57	0.67	5.6	10	0	1
PSP3.84	PS	5.14	2.69	0.57	3.84	0.67	5.6	10	0	1
PSP4.34	PS	6.67	3.04	0.43	4.34	0.67	5.6	10	0	1
PSP5.14	PS	9.23	3.6	0.31	5.14	0.67	5.6	10	0	1
ESP2.62	ES	1.82	1.84	2.12	2.62	0.67	5.6	10	0	1
PSP3.76	PS	3.86	2.66	0.96	3.76	0.67	5.6	10	0	1
PSP4.75	PS	6.61	3.33	0.52	4.75	0.67	5.6	10	0	1
PSP5.54	PS	9.15	3.88	0.37	5.54	0.67	5.6	10	0	1
PSP6.27	PS	11.82	4.39	0.29	6.27	0.67	5.6	10	0	1
ESP1.56MU	ES	1.04	1.1	2.31	1.56	0.3, 0.5, 0.67, 1.0, 1.5	5.6	10	0	1
PSP3.84MU	PS	5.14	2.69	0.57	3.84		5.6	10	0	1
ESP1.56RHO	ES	1.04	1.1	2.31	1.56	0.67	1.0, 2.0, 3.0, 4.0 5.6	10	0	1
ESP2.57RHO	ES	2.16	1.8	1.44	2.57	0.67		10	0	1
PSP3.84RHO	PS	5.14	2.69	0.57	3.84	0.67		10	0	1
ESP1.88PHI	ES	1.62	1.32	1.37	1.88	0.67	5.6	10	0, 15, 30 ,45	1
PSP2.17PHI	PS	2.50	1.52	0.77	2.17	0.67	5.6	10		
ESP1.56As$_b$	ES	1.04	1.1	2.31	1.56	0.67	5.6	10	0	1, 2, 3, 4 (w_b/l_b)
	ES	1.04	1.1	2.31	1.56	0.67	5.6	10	0	1, 2, 3, 4 (h_b/l_b)

3. Interpretation of results

3.1 Impact dynamics

3.1.1 Block transport modes

Blocks can be transported under partially and entirely submerged conditions. In the partially submerged mode, the flow height is less than the block height (i.e., $h_{\mathrm{f}} < h_{\mathrm{b}}$). In the entirely submerged condition, the flow height exceeds that of the block (i.e., $h_{\mathrm{f}} \geq h_{\mathrm{b}}$). Figure 3a and b show typical snapshots of the kinematics of the flows transporting a block for entirely and partially submerged cases, respectively.

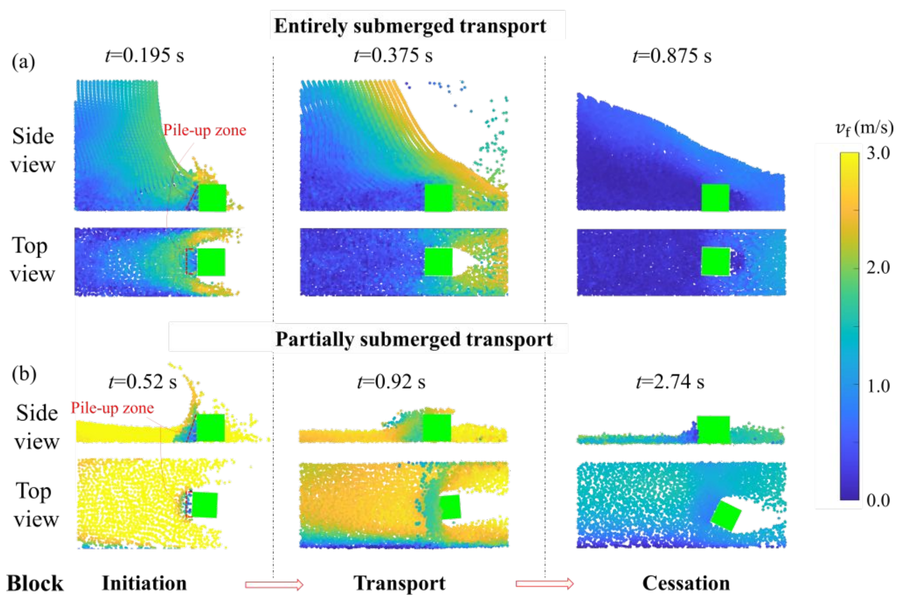

Figure 3. Typical snapshots of the frontal kinematics of the computed flows transporting the block. (a) Entirely submerged transport mode, which is observed from Test ESP1.56; and (b) partially submerged transport condition, which is observed from Test PSP3.12. v_{f} is the flow velocity.

It can be observed that, in both transport modes, a pile-up zone characterized by near-zero flow velocity forms behind the block as the flow initiates the motion of the block, inducing an earth pressure on the block. Note that, in the entirely submerged transport mode, a pile-up zone in front of the block progressively emerges as the block is transported. However, no pile-up zone in front of the block develops throughout the partially submerged transport process.

The differences in flow depth and pile-up zone evolution between entirely and partially submerged transport modes result in different mechanisms for incipient motion and travel distance of impacted blocks.

Specifically, in the entirely submerged mode, flow material overruns the top of the block, forming a high-velocity layer above it. This induces a normal load on the block, mobilising block friction to limiting acceleration and runout. Conversely, in the partially submerged mode (e.g., Test PSP3.12), only the lower portion of the block is inundated initially. Flow is then deflected laterally without overflow, creating a pronounced bow shock (Liang et al., 2023) and clear separation between the high-velocity surface and stagnant rear zone. The lack of material on the block crest reduces normal stress and basal friction, enabling greater acceleration and longer runout for the same flow discharge. These differences require separate analysis to predict threshold conditions and travel distances for blocks impacted by flow-type landslides in natural settings.

3.1.2 Motion threshold

Momentum flux, defined as the product of flow velocity squared and flow depth, $h_\mathrm{f}v_\mathrm{f}^2$, represents the dynamic impact intensity of a flow-type landslide. Physically, it combines the inertial force of the moving mass with the geometric effect of flow depth, providing a more comprehensive measure of the destructive potential than either velocity or depth alone (Prieto et al., 2018). In engineering applications, momentum flux has become a widely adopted hazard parameter for assessing building vulnerability because it directly correlates with the initiation of structural motion and progressive failure. It allows engineers and emergency managers to predict whether a building will remain stable, slide, or overturn under impact, which is critical for designing setback distances and prioritizing search and rescue zones. Thresholds of momentum flux are selected empirically by analyzing observed damage from field cases, back-calculating flow depths and velocities at damaged sites, and fitting fragility curves using lognormal distributions. Median values for damage states are derived from spatial patterns of inundation and building responses, accounting for variability in construction types.

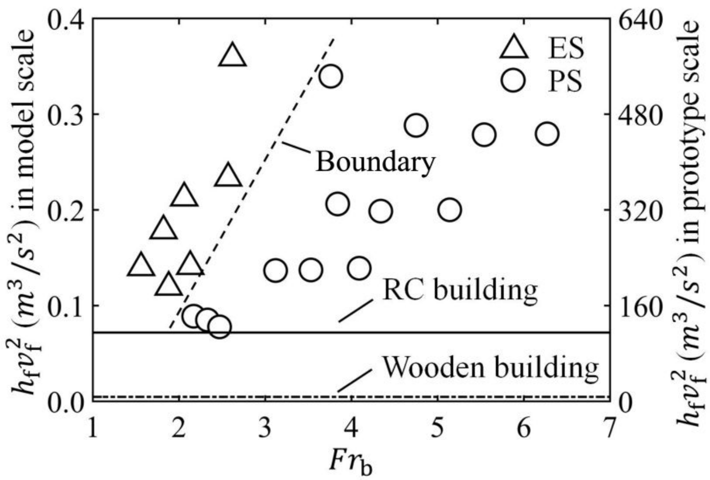

Figure 4. Momentum flux ($h_f v_f^2$) threshold to initialize the block under flow impact. 'ES' indicates the entirely submerged mode and 'PS' indicates the partially submerged mode. RC building means reinforced-concrete buildings. The inclined dash line, named Boundary, represents the transition boundary between the entirely submerged mode and the partially submerged mode.

Figure 4 shows the momentum flux $h_f v_f^2$ thresholds of flow-type landslide fronts against the simulated motion response of building-like blocks against the impact Froude number Fr_b. The thresholds, the solid and dash horizontal lines, represent the minimum dynamic momentum flux h_f v_f^2 required to trigger structural destabilisation and loss of foundation restraint in flow-type landslide (Kean et al., 2019). Two critical thresholds are marked: a solid line at 115 m^3/s^2 (0.072 m^3/s^2 in model) for RC structures (Luo et al., 2022) and a dashed line at 7.1 m^3/s^2 (0.0045 m^3/s^2 in model) for wooden structures (Kean et al., 2019). All 20 cases in this study lie above both thresholds, spanning 120~600 m³/s² in prototype scale, in line with that all block has been displaced in simulations.

An inclined dashed line (Boundary, the separating line constructed by Support Vector Machine (Cortes and Vapnik, 1995) divides the plot into ES and PS regions (left zone and right zone). Physically, this demonstrates how submergence modulates the block's motion resistance: for a given Fr_{b}, the ES mode enables mobilization more readily than the PS mode. This is shown in the clustering of ES data points (triangles) at lower momentum flux values relative to a same Fr_{b}, implying that deeper flows promote block motion. Consequently, a small increment in Fr_{b} under entirely submerged conditions induces a larger increment in momentum flux, rendering structures more susceptible to motion.

3.2 Scaling relationships of flow-block interaction

3.2.1 Basal friction of block

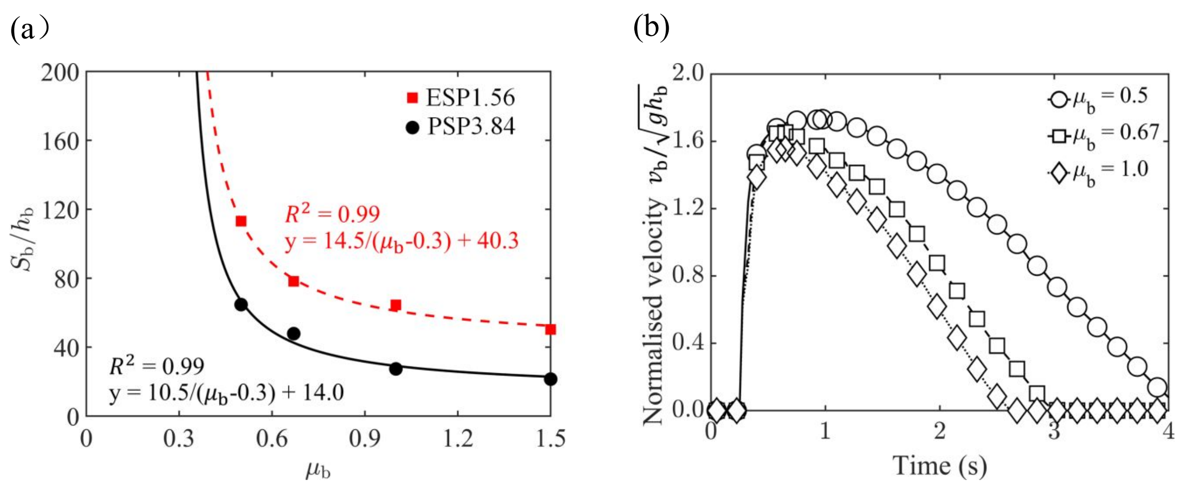

Figure 5. Influence of basal frictional coefficient μ_{b} on block kinematics: (a) the effect of basal frictional coefficient between block bottom and flume bed on normalized travel distance (run ESP1.56 and PSP3.84); (b) the effect of basal frictional coefficient between block bottom and flume bed on scaled block velocity, $v_{\mathrm{b}}/\sqrt{gh_{\mathrm{b}}}$ (run ESP1.56).

Figure 5a shows the empirical relationship between basal friction coefficient μ_b and dimensionless travel distance S_b/h_b for a block under two numerical conditions (ESP1.56 and PSP3.84). A strong inverse proportionality can be observed, specifically higher friction markedly reduces travel distance. The evident inversely proportional regression (i.e., coefficient of determination (R^2) of 0.99 for both ESP1.56 and PSP3.84) validates the observed trend and provides a reliable predictive tool within the tested parameter space. This relationship is particularly pronounced at lower friction values (μ_b < 1.0), where a modest increase in friction leads to a substantial reduction in displacement. For instance, in run ESP1.56, increasing μ_b from 0.5 to 1.0 reduces the travel distance by approximately 58%. Beyond this range, the curve begins to flatten, suggesting a point of diminishing returns where further increases in friction yield progressively smaller reductions in travel distance. As the friction coefficient approaches a critical threshold (0.3), the maximum resistive force becomes insufficient to counteract the continuous driving forces. These forces and persistent earth pressure, create a perpetual net positive force on the block.

The inverse relationship between dimensionless travel distance and basal friction coefficient stems from the kinematics of the block motion post-impact. Figure 5b shows the normalized velocity of a block against time for three distinct basal friction coefficients μ_b: 0.5, 0.67, and 1.0. All three blocks initiate motion simultaneously, undergoing a rapid acceleration phase where velocity quickly peaks. The maximum normalized velocities attained are clustered within a narrow range, approximately 1.58 to 1.72. This similarity suggests that the blocks gain comparable maximum kinetic energy, irrespective of μ_b. The brief duration of this acceleration implies that the work done by the initial impact force is dominant, far exceeding the resistance from friction during the acceleration interval. Friction becomes the governing force, resulting in a near-constant negative acceleration (linear velocity decay) until the blocks come to rest. As expected, higher friction coefficients lead to steeper deceleration and a shorter total duration of motion.

This explains the observed inversely proportional relationship, where higher friction yields stronger deceleration and shorter distances, as captured in the empirical fit function. Consequently, given that the maximum kinetic energy is comparable across all three cases, the total sliding distance achieved during the deceleration phase is inversely proportional to the basal friction coefficient μ_{b}. For rapid rescue after a landslide event, enhancing basal friction via building materials, such as opting for textured concrete foundations (typically 0.3~0.7 on soils) over wood (0.2~0.5), can substantially reduce travel distance of building.

3.2.2 Density ratio

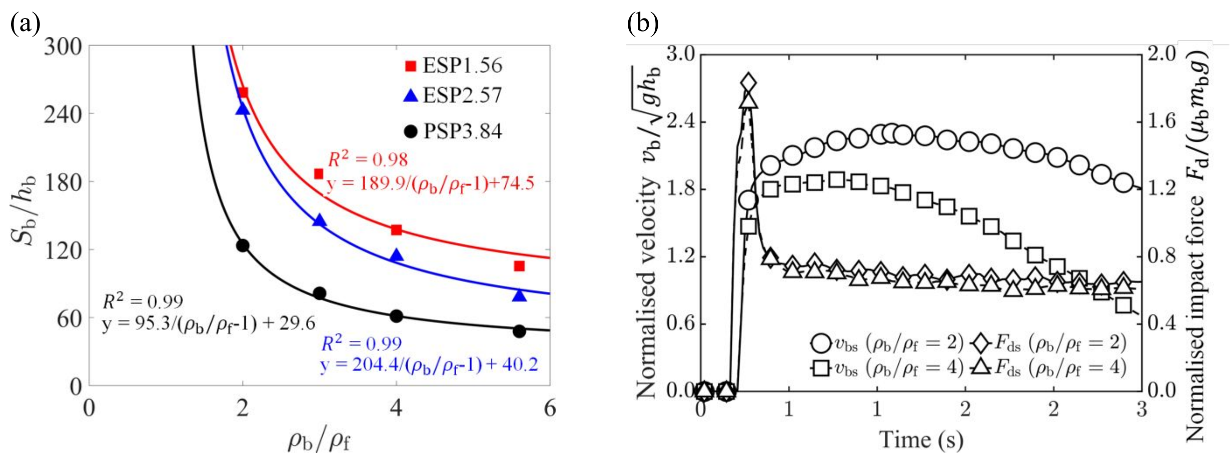

Figure 6. (a) The effects of density ratio on normalized travel distance of a block (runs ESP1.56, ESP2.57 and PSP3.84); and (b) The effect of density ratio on impact force and block velocity. v_{bs} is normalized travel velocity of block, $v_{\mathrm{b}}/\sqrt{gh_{\mathrm{b}}}$. F_{ds} is the normalized impact force on block from flow-type landslide, $F_{\mathrm{d}}/(\mu_{\mathrm{b}}m_{\mathrm{b}}g)$, where m_{b} is the mass of the block.

Figure 6 (a) illustrates the relationship between the density ratio $\rho_{\mathrm{b}}/\rho_{\mathrm{f}}$ and the dimensionless travel distance ($S_{\mathrm{b}}/h_{\mathrm{b}}$) under three different conditions. A strong inverse relationship is evident across all three datasets: as the density ratio, $\rho_{\mathrm{b}}/\rho_{\mathrm{f}}$, increases, its travel distance markedly decreases. Figure 6 (b) shows the time-histories of block velocity and impact force for blocks with two typical density ratios ($\rho_{\mathrm{b}}/\rho_{\mathrm{f}}$): 2 and 4. The impact force profiles exerted by the flow-type landslide are nearly identical for both cases. However, the velocity curves differ significantly due to inertia. The higher-density block (ρ_b/ρ_f = 4) has greater mass, which resists acceleration, resulting in a much lower peak velocity (about 1.9) compared to the block with ρ_b/ρ_f = 2, which is about 2.3. In the subsequent deceleration phase, while the sustained impact forces remain comparable, the block with ρ_b/ρ_f = 2 experiences a smaller basal friction force because of lower mass. This results in a net deceleration of a smaller magnitude (a less steep velocity slope) than the high-density block. Consequently, the low-density block combines a higher maximum velocity with a slower deceleration, confirming a strong inverse relationship between block density and total sliding distance. For instance, Figure 6 (a) shows in the ESP2.57 condition (red squares), increasing the density ratio from 2 to 4 reduces the travel distance by approximately 47%, from 258 to 137.

This relationship has practical value in post-disaster response. Given estimates of the density of an object, and density and energy (to select the correct predictive curve between entirely submerged mode and partially submerged mode) of a landslide, the model can be used to predict its final location. This allows search and rescue teams to focus on high-probability zones along the flow path, greatly improving efficiency and speed.

3.2.3 Initial impact orientation of block

Figure 7a shows the critical influence of block orientation angle (φ) on normalized travel distance when impacted by a flow-type landslide. For both entirely submerged (ESP1.88) and partially submerged (PSP2.17) conditions, the normalized travel distance is the maximum when φ=0° (head-on impact) and decreases steadily when φ = 30° (oblique impact). This trend reflects the reduction in effective normal force and the increase in lateral deflection, which promote rotational instability and energy dissipation via asymmetric contact (Liu et al., 2025).

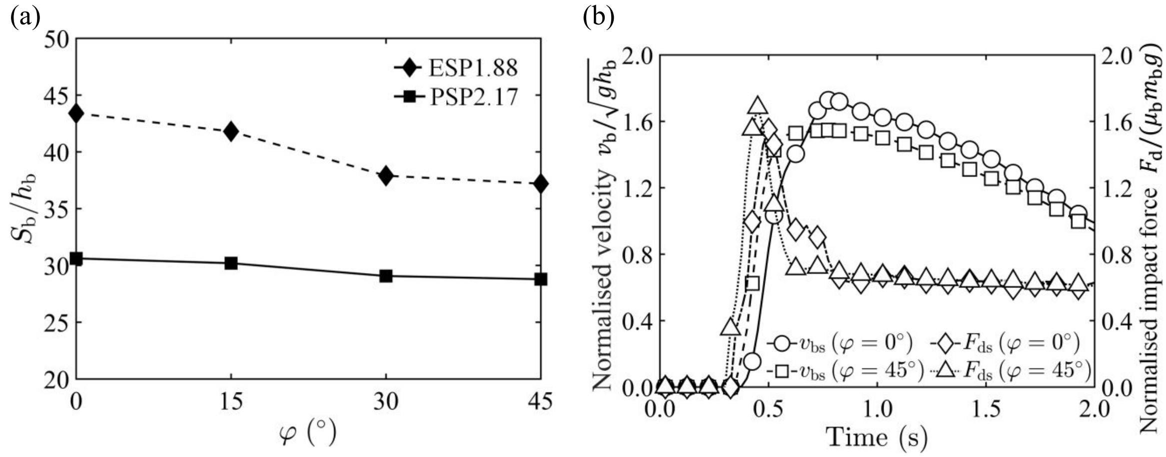

Figure 7. (a) Effect of initial block impact orientation φ on normalized travel distance of block; (b) the different in velocity and impact force on block when changing initial orientation of block (ESP1.88). v_{bs} is normalized travel velocity of block, $v_b/\sqrt{gh_b}$. F_{ds} is the normalized impact force on block, $F_d/(\mu_b m_b g)$.

Figure 7b shows normalized block velocity and normalized impact force exerted by the flow, comparing two scenarios: a block at φ= 0° orientation and one at φ= 45°. A key feature is that the block at 45° orientation initiates acceleration slightly earlier than the block at 0° orientation. Furthermore, the 45° block experiences a slightly higher peak impact force (F_{ds}=1.6) compared to the 0° case (F_{ds}=1.45). This arises because the 45° orientation presents a larger projected frontal area, capturing greater momentum, given that mass and basal friction are constant. However, the impact force on the 0° block is sustained for a longer duration after its initial peak. This prolonged application of force (greater impulse) allows the 0° block to ultimately achieve a higher maximum velocity than the 45° block, despite the latter's earlier acceleration. In the subsequent deceleration phase, the velocity curves for both orientations exhibit nearly parallel slopes. This indicates that the net retarding force, resulting from the combination of the basal friction and the residual impact force, is comparable in both cases. Consequently, having initiated this phase from a higher peak velocity, the 0° block traverses a longer total sliding distance before coming to rest.

From an engineering perspective, orienting structures at an oblique angle (e.g., 45°) to the expected flow direction can reduce displacement and impact loads, enhancing safety. Head-on orientation should be avoided in hazard zones. For search and rescue, when a target's initial orientation is unknown, this model provides bounds for the probable travel distance: the upper bound from the head-on (φ= 0°) case and the lower bound from the oblique (φ= 45°) case, narrowing the search zone.

3.2.4 Influence of aspect ratio of block on travel distance

Figure 8(a) shows the effect of block aspect ratio on normalized travel distance. Travel distance decreases monotonically with increasing aspect ratio for both height-to-width ($h_\mathrm{b}/l_\mathrm{b}$) and width-to-length ($w_\mathrm{b}/l_\mathrm{b}$) ratios, consistent with Liu et al. (2025). At high aspect ratios (e.g., 4), $h_\mathrm{b}/l_\mathrm{b}$ produces slightly shorter travel distances than $w_\mathrm{b}/l_\mathrm{b}$, indicating height-oriented elongation reduces sliding marginally more than length-oriented elongation. For aspect ratios ≤ 2.31, impact force amplitude scales with the increase in force-bearing area for both orientations. Above this threshold, tall blocks enter a partially submerged mode, so the height increase contributes less to impact force than equivalent length increases.

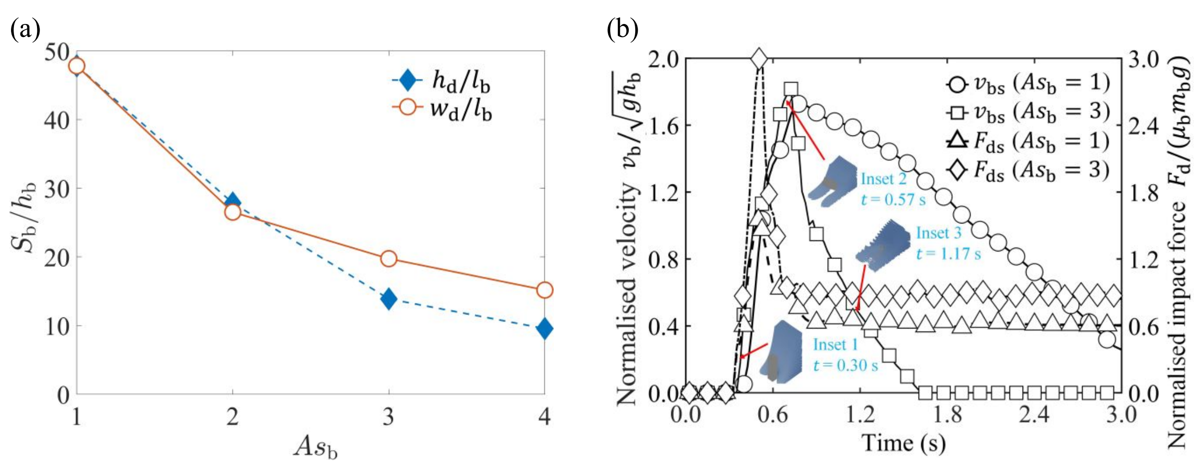

Figure 8. The effect of aspect ratio of block on the block kinematics: (a) the effect on normalized travel distance of block (the flow condition is ESP1.56; and (b) the effect on velocity of block

(Insets 1~3 show the process of block overturning) when the block has a h_b/l_b ratio of 1 and 3. As_b is the aspect ratio of block. v_{bs} is normalized velocity of block, $v_b/\sqrt{gh_b}$. F_{ds} is the normalized impact force on block, $F_d/(\mu_b m_b g)$.

Figure 8(b) compares normalized velocity and normalized impact force for a square block (h_b/l_b = 1) and a tall block (h_b/l_b = 3). The tall block experiences a peak impact force (F_{ds}= 3) nearly twice that of the square block (F_{ds}=1.6) and shows steeper acceleration and deceleration slopes. The velocity profile of the tall block is distinct, exhibiting a steeper slope during both acceleration and deceleration compared to the square block. This behavior is attributed to a complex motion combining sliding with overturning, as illustrated by the 3 insets. Inset 1 (t=0.30s) shows the initial impact. Inset 2 (t=0.57s) captures the block in the process of toppling, corresponding to the peak velocity and force. Inset 3 (t=1.17s) shows the block after it has completely overturned, with its long axis falling onto the bed, leading to its rapid cessation of motion as it is subsequently buried by the flow.

Shape sensitivity has major implications for search operations: flat, squat objects (e.g., vehicles, containers, slabs) are transported significantly farther than cubic or tall objects. Search radii for these mobile shapes should be expanded to account for their greater displacement potential.

3.2.5 Relative importance of governing parameters

Since the individual effects of each parameter are presented before, a systematic comparison of their relative importance is necessary to better understand the controlling factors of block displacement. Table 4 summarizes the maximum variation in normalized travel distance associated with each parameter over its tested range.

Among the four parameters, aspect ratio produces the largest effect. Squat blocks (aspect ratio $\leq$ 1) travel up to five times farther than slender blocks (aspect ratio = 3). This substantial difference stems not only from changes in resistance but also because aspect ratio significantly influences the motion mode of the block. Slender blocks are more prone to early overturning, which terminates their motion, whereas squat blocks tend to sustain sliding over longer distances.

Basal friction and density ratio also exert strong influences, reducing normalized travel distance by up to 85% and 82%, respectively, mainly through increased frictional energy dissipation after impact. In comparison, initial orientation has a relatively moderate effect, with head-on (0°) impacts resulting in approximately 30% longer travel distances than 45° oblique impacts due to longer momentum transfer before rotation begins.

Table 4. Maximum variation in normalized travel distance caused by each governing parameter over the tested range

Parameters	Range	Maximum Change
Basal friction	0.3~1.5	85%
Density ratio	1.0~5.6	82%
Initial orientation	0°~45°	30%
Aspect ratio	1.0~3.0	More than 400%

3.2.6 Travel distance of impacted blocks in different submerged modes

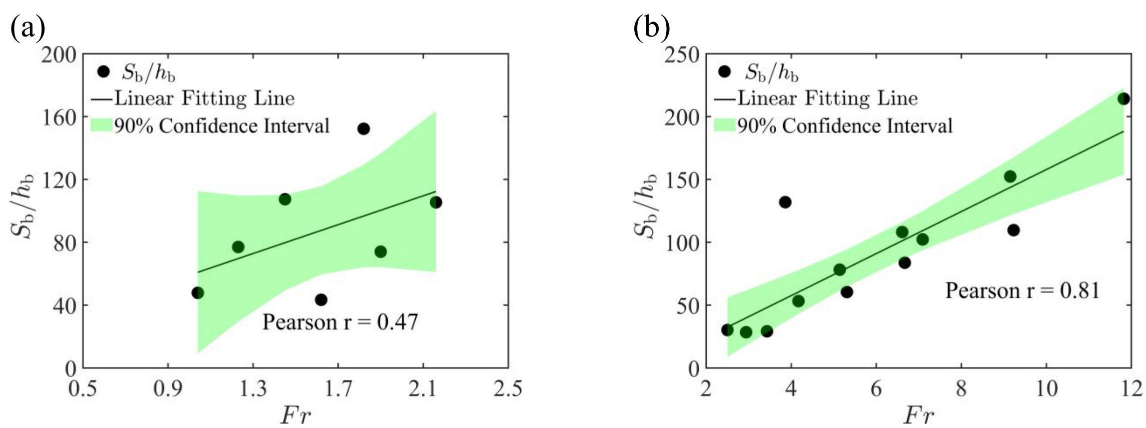

(c)

(d)

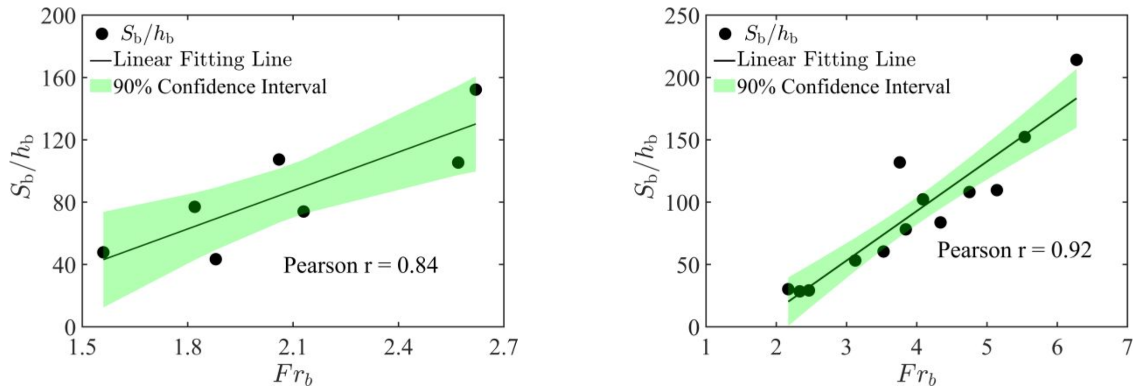

Figure 9. Correlations between the normalized travel distance of displaced blocks and the impact dynamics of flow-type landslides on blocks. The impact dynamics is characterized by using different dimensionless numbers: Froude number Fr for (a) entirely and (b) partially submerged transport modes; impact Froude number Fr_b for (c) entirely and (d) partially submerged transport modes.

Figure 9 compares two dimensionless parameters (i.e., the Froude number Fr and the impact Froude number Fr_b) in predicting normalized travel distance (S_b/h_b) of blocks under entirely and partially submerged conditions. While a higher flow Froude number tends to increase travel distance (Zainali et al., 2015), Feng, (2024) did not quantify this relationship; thus, it is used here as a reference baseline (Figure 9a and 9b).

A direct comparison reveals the superior predictive power of the impact Froude number Fr_b. For entirely submerged blocks (Figure 9a vs. 9c): The Froude number in (a) exhibits a weak correlation (Pearson r = 0.51) with widely scattered data and broad confidence intervals. In contrast, the impact Froude number (Figure 9c) shows a strong, well-defined linear trend (Pearson r = 0.84), indicating a much more reliable predictive relationship. For partially submerged blocks (Figure 9b vs. 9d): This trend is further confirmed. While the Froude number in (b) offers a reasonable correlation (r = 0.81), the impact Froude number in (d) provides an exceptionally strong correlation (r = 0.92), with data points tightly clustered around the fitting line. As a result, a semi-empirical model for predicting the transport distance of the blocks displaced under flow impact can be obtained by the computed data:

$$S_b/h_b = \begin{cases} 38.9Fr_b - 61.1 & (h_b > h_f) \\ 84.3Fr_b - 90.0 & (h_b \le h_f) \end{cases} \tag{11}$$

As shown in Eq. 11, the impact Froude number (Fr_b) integrates both flow dynamics and geometric scaling between h_f and block height h_b. An increase in Fr_b (e.g., via higher flow velocity or smaller h_b) amplifies the impact force on the block, as the kinetic energy of flow outweighs gravitational stabilization. This reduces the block resistance to impact force, resulting in greater normalized travel distance (S_b/h_b). Conversely, a decrease in strengthens block resistance through enhanced gravitational effects, limiting energy transfer from the flow and confining to shorter distances. In essence, impact Froude number (Fr_b) is a ratio of driving forces to resisting forces (gravity-induced friction between the block base and the flume bed).

The primary implication is that impact Froude number greatly improves the accuracy of predicting block travel distance compared to the Froude number. This higher predictive power is critical in post-disaster scenarios: for locating submerged vehicles or containers, a model based on impact Froude number, can sharply narrow the probable search area, enabling search-and-rescue teams to concentrate resources, saving valuable time and effort. The semi-empirical model reliably predicts normalized block travel distance for impact Froude numbers from 1.0 to 6.3 in both entirely and partially submerged modes. The relationship holds for dry granular flows.

3.3 Guiding tool for mobile blocks displaced and buried by granular flows

Among the parameters investigated, the impact Froude number, basal friction coefficient, and density ratio were selected for the contour analysis because they not only produce substantial individual effects but also exhibit clear interactions in controlling normalized travel distance. These parameters can also be more readily estimated or inferred from event characteristics and terrain conditions in post-disaster scenarios, making them suitable for developing a practical predictive tool. In contrast, although block aspect ratio exerts a strong influence on travel distance, it primarily affects the dominant motion mode of the block. For example, whether the block tends to slide for a longer distance or overturns earlier, thereby arresting its motion. This mode-shifting effect is more categorical and object-specific rather than a continuous modulating factor. Therefore, the influence of aspect ratio is best accounted for separately once the object type (e.g., squat vs. slender) is identified, while the contour charts focus on the three parameters that offer the greatest utility for rapid, field-applicable estimation across varying flow and interface conditions.

3.3.1 Contour line based on impact Froude number, frictional coefficient

Figure 10 presents a contour map illustrating the normalized travel distance S_b/h_b as a function of two dimensionless parameters: the impact Froude number Fr_b and the basal friction coefficient μ_b. The plot differentiates between two transport modes: entirely submerged (dashed lines, 1< Fr_b < 3) and partially submerged (solid lines, 1< Fr_b < 6). The contours clearly demonstrate the governing physics: for any given friction coefficient (moving horizontally along the x-axis), an increase in the impact Froude number results in a significantly longer travel distance (crossing contours to higher values). This is because the impact Froude number represents the impact energy on block.

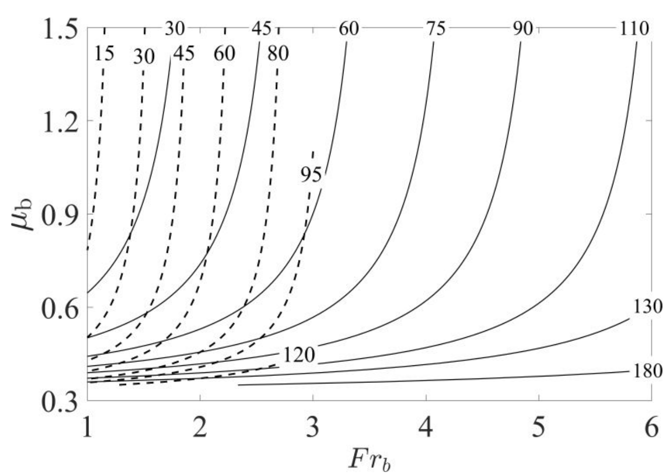

Figure 10. Chart designed for quickly locating the normalized travel distance S_b/h_b of block with different basal friction coefficient μ_b in a flow-type landslide. (Density ratio ρ_b/ρ_f is 5.6; the solid line zone is contour line of partially submerged data, and the dash line zone is contour line of entirely submerged data)

The contours demonstrate the governing physics: for a fixed friction coefficient (traversing horizontally), an increase in Fr_b leads to longer travel distances, as higher impact forces propel the block farther. Conversely, increasing μ_b (traversing vertically in Figure 10) reduces distances due to rapid energy dissipation.

3.3.2 Contour line based on impact Froude number, density ratio

Figure 11 presents contour plots of the normalized travel distance, S_b/h_b, as a function of the dimensionless parameters impact Froude number Fr_b (horizontal axis, ranging from 1 to 6) and density ratio ρ_b/ρ_f (vertical axis, ranging from 1 to 6). The plot distinguishes between two transport modes: entirely submerged and partially submerged. The contours demonstrate the governing physics: for a fixed density ratio (traversing horizontally), an increase in Fr_bleads to longer travel distances, as higher impact forces propel the block farther. Conversely, increasing ρ_b/ρ_f (traversing vertically) reduces distances due to greater inertial resistance.

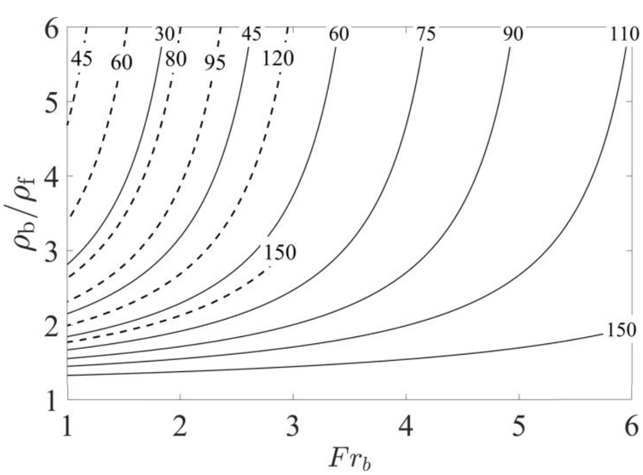

Figure 11. Chart designed for quickly locating the normalized travel distance $S_{\mathrm{b}}/h_{\mathrm{b}}$ of block with different density ratio $\rho_{\mathrm{b}}/\rho_{\mathrm{f}}$ in a flow-type landslide. (Basal friction coefficient μ_{b} is 0.67; the solid line zone is contour line of partially submerged data, and the dash line zone is contour line of entirely submerged data).

A critical finding in both Figure 10 and Figure 11 is the distinction between the two modes. In the entirely submerged regime, the contour lines are densely packed. This indicates that the travel distance is highly sensitive to small variations in both friction and the impact Froude number. A minor change in either parameter leads to a large change in the resulting distance. Conversely, in the partially submerged regime, the contours are widely spaced, signifying a more stable relationship where the travel distance is less sensitive to the same variations in input conditions.

This contour map serves as a powerful predictive tool for forecasting the travel distance of displaced objects in hazard assessment and emergency response. For post-disaster recovery, this chart is invaluable for locating critical infrastructure or vehicles. By estimating the event's hydraulic characteristics (to find the impact Froude number Fr_{b}) and the terrain's properties (to determine μ_{b} and $\rho_{\mathrm{b}}/\rho_{\mathrm{f}}$), rescue teams can use this map to read the corresponding contour value. The contour map provides a practical and rapid tool for estimating the displacement of mobile non-spherical objects in dry-phase flow. The model is valid for impact Froude numbers ranging from 1.0 to 6.0, basal friction coefficients of 0.3–1.5, and density ratios of 1.0–5.6, covering both entirely and partially submerged transport modes on a typical alluvial fan slope of $10°$. These ranges are representative of many real-world events affecting low-rise structures and vehicles in mountainous regions.

Limitations

While the coupled MPM-SDEM framework and the proposed semi-empirical model provide valuable insights into the displacement mechanisms of non-spherical objects in flow-type landslides, several limitations should be acknowledged to ensure appropriate application of the findings.

First, the numerical simulations were conducted under dry granular flow conditions using glass beads with a uniform particle size. Real-world flow events often involve multi-phase flows containing water, fine sediments, and a wide range of grain sizes, which can significantly alter buoyancy, drag, and energy dissipation. Consequently, the predicted travel distances and the applicability of the contour charts may differ in water-saturated debris flows. Second, all simulations considered a single block on a fixed channel slope of 10°. In natural settings, multiple objects may interact with each other and with the surrounding terrain, and slopes in deposition zones can vary considerably. These interactions and topographic variations were not captured in the present study and may influence both initiation thresholds and final burial locations. Third, the semi-empirical relationship and contour maps are strictly valid within the tested parameter ranges: impact Froude numbers of 1.04–6.27, basal friction coefficients of 0.3–1.5, and density ratios of 1.0–5.6. Extrapolation beyond these ranges, particularly for very high-velocity surges or extremely light or heavy objects, should be performed with caution. Furthermore, the model was developed using a geometric scale factor of 40 under Froude similarity. Although this scaling is widely accepted for granular flows, full-scale field validation against documented landslide events remains necessary to confirm the transferability of the results.

While the single flume experiment in Appendix A offers a valuable benchmark for calibrating the fluid–solid interface parameters, it is limited to one block geometry (cube), one high-density material (copper), and the dry flow condition. This represents a methodological limitation, given that the subsequent parametric study covers a much wider range of block densities, aspect ratios, initial orientations, and both entirely and partially submerged conditions. Nevertheless, we note that this experiment itself constitutes a contribution: to the best of our knowledge, it is the first to successfully capture the full kinematics (including rotation) of an object impacted and potentially buried by a granular flow using bottom-view imaging through a transparent flume bed. Such data are extremely rare due to the opacity of dense granular flows. Future experimental work covering a broader range of densities, geometries, and submersion conditions would further strengthen the validation of the model.

Future work will aim to extend the current framework in several directions. The model will be expanded to multi-phase flows to account for the effects of water and fine particles on object transport. Interactions among multiple objects and more variable topographic conditions will also be considered. In addition, full-scale field validation against documented events and more rigorous numerical uncertainty quantification are needed to strengthen the reliability and transferability of the proposed relationships. Finally, combining the mechanistic understanding developed in this study with data-driven approaches may help create more generalized tools applicable to a wider range of real-world landslide scenarios.

Conclusions

In this study, the impact mechanisms between flow-type landslide and mobile block are revealed with a high-fidelity MPM-SDEM solver. Based on the findings, guiding tools were developed to determine the potential positions of displaced and buried objects. The effects of impact angle, basal friction, and block aspect ratio were systematically investigated. The key conclusions are:

(1) A block can be transported in an entirely submerged or partially submerged mode, depending on the relationship between the flow and block heights. Compared to the partially submerged mode, the entirely submerged mode exhibits a lower threshold in terms of incident momentum flux for

initiating block instability and subsequent displacement. For the same impact Froude number, full submergence yields greater momentum flux due to larger flow depth. From a practical perspective, if the pre-impact flow depth or the final deposition depth can be estimated (e.g., from field traces, high-water marks, or numerical inundation modeling), the flow-depth ratio provides a useful indicator for search zone delineation. Blocks that experience entirely submerged transport are expected to have the longer travel distances, with normalized displacement increasing steeply with impact Froude number.

(2) The impact Froude number effectively characterizes block travel distance in both submerged and partially submerged conditions. Normalized displacement increases linearly with impact Froude number because this dimensionless group represents the ratio of the flow's inertial kinetic energy to the gravitational resistance of block. A higher impact Froude number enhances the efficiency of momentum transfer from the flow to the block before significant frictional dissipation occurs during the post-impact deceleration phase, resulting in longer runout. When a high impact Froude number can be inferred before or shortly after impact, objects are expected to travel substantially farther downstream. Search teams should therefore expand the prioritized zone significantly farther along the flow path, rather than concentrating near original locations, to improve efficiency within the critical 72-hour window.

(3) This study quantified the key parameters controlling block travel distance. Increasing basal friction from 0.3 to 1.5 and the density ratio from 1.0 to 5.6 reduces normalized travel distance by 60–85% and 82%, respectively. Block geometry also plays an important role: head-on (0°) impacts result in about 30% longer travel distances than 45° oblique impacts because of longer momentum transfer before rotation begins. Squat blocks (aspect ratio ≤ 1) travel up to five times farther than slender ones (aspect ratio = 3) because their lower center of mass provides stronger resistance to overturning. These outcomes suggest that if we know the impact direction, we can have a sense as

to the displaced or burial distance of objects relative to each other. This may offer clues for disaster reconstruction.

(4) A guiding tool based on the impact Froude number, basal friction coefficient and density ratio of block is proposed to determine the normalized travel distance for both partially and entirely submerged blocks. In submerged regimes, small changes in impact Froude number or basal friction coefficient yield large changes in travel distance due to amplified kinetic transfer and rapid dissipation. Partial submergence offers greater robustness to parameter uncertainty. The tool enables disaster managers to forecast travel zones quickly, scaling for density ratio to avoid underestimations for lighter objects, which is critical for effective search-and-rescue deployment.

To support rapid decision-making in post-disaster search and rescue, the following operational guidelines can be applied using the impact Froude number and contour charts developed in this study. Rescue team can first estimate flow velocity and depth (to compute the impact Froude number) and assess whether the object is entirely or partially submerged. In entirely submerged conditions, predicted travel distances are highly sensitive to small changes in impact Froude number or basal friction; therefore, a wider downstream search corridor should be adopted initially. Low-density objects (density ratio = 1–2) travel substantially farther than dense structures (travel distance can be reduced by up to 82% only when the density ratio reaches 5.6), so lighter debris such as wooden fragments or vehicles warrants priority searching farther along the flow path. Objects oriented head-on to the flow ($\varphi = 0°$) are displaced approximately 30% farther than those at oblique angles (45°), increasing the required search distance. Squat or low-aspect-ratio objects (aspect ratio ≤ 1) travel up to five times farther than slender ones before overturning arrests motion. By combining these rules with the contour charts and the semi-empirical relation, teams can quickly define high-probability search zones from limited field observations and allocate limited resources more effectively within the critical 72-hour survival window.

Acknowledgments

The paper acknowledges the financial support obtained from Collaborative Research Fund (C7085-24G) of the Research Grants Council of Hong Kong.

Conflict of Interest Statement

The authors declare no conflicts of interest.

Data availability

Data generated or analyzed during this study are available from the corresponding author upon reasonable request.

References

Agarwal, S., Karsai, A., Goldman, D.I., Kamrin, K., 2021. Surprising simplicity in the modeling of dynamic granular intrusion. Sci. Adv. 7(17), eabe0631.https://doi.org/10.1126/sciadv.abe0631

Blatny, L., Gaume, J., 2025. Matter (v1): an open-source MPM solver for granular matter. Geosci. Model Dev. 18, 9149 – 9166. https://doi.org/10.5194/gmd-18-9149-2025

Buckingham, E., 1914. On physically similar systems; illustrations of the use of dimensional equations. Phys. Rev. 4(4), 345–376. https://doi.org/10.1103/PhysRev.4.345.

Ceccato, F., Redaelli, I., di Prisco, C., Simonini, P., 2018. Impact forces of granular flows on rigid structures: comparison between discontinuous (DEM) and continuous (MPM) numerical approaches. Comput. Geotech. 103, 201–217. https://doi.org/10.1016/j.compgeo.2018.07.014.

Ceccato, F., Yerro, A., Di Carluccio, G., 2024. Simulating landslides with the material point method: Best practices, potentialities, and challenges. Engineering Geology 338, 107614. https://doi.org/10.1016/j.enggeo.2024.107614

Chehade, R., Chevalier, B., Dedecker, F., Breul, P., Thouret, J.C., 2021. Discrete modelling of debris flows for evaluating impacts on structures. Bull. Eng. Geol. Environ. 80(8), 6629–6645. https://doi.org/10.1007/s10064-021-02278-3.

Choi, C.E., Cui, Y., Liu, L.H.D., Ng, C.W.W., Lourenço, S.D.N., 2017. Impact mechanisms of flow-type landslide against curved barriers. G é otech. Lett. 7(4), 330–338. https://doi.org/10.1680/jgele.17.00094.

Collins, G.S., Melosh, H.J., 2003. Acoustic fluidization and the extraordinary mobility of sturzstroms. J. Geophys. Res. Solid Earth 108(B10). https://doi.org/10.1029/2003JB002465.

Cortes, C., Vapnik, V., 1995. Support-vector networks. Machine Learning 20, 273–297. https://doi.org/10.1007/BF00994018

Cui, M., Chen, F., Bu, F., 2021. Multiphase theory of granular media and particle simulation method for projectile penetration in sand beds. Int. J. Impact Eng. 157, 103962. https://doi.org/10.1016/j.ijimpeng.2021.103962.

Cuomo, S., 2020. Modelling of flowslides and debris avalanches in natural and engineered slopes: a review. Geoenviron. Disasters 7(1), 1. https://doi.org/10.1186/s40677-019-0133-9.

De Haas, T., Braat, L., Leuven, J.R.F.W., Lokhorst, I.R., Kleinhans, M.G., 2015. Effects of debris flow composition on runout, depositional mechanisms, and deposit morphology in laboratory experiments. J. Geophys. Res. Earth Surf. 120(9), 1949–1972. https://doi.org/10.1002/2015JF003525.

Doran, D., Cather, B. (Eds.), 2013. Construction materials reference book. Routledge. https://doi.org/10.4324/9780080940380.

Drucker, D.C., Prager, W., 1952. Soil mechanics and plastic analysis or limit design. Q. Appl. Math. 10(2), 157–165. https://doi.org/10.1090/qam/48291.

Dunatunga, S., Kamrin, K., 2015. Continuum modelling and simulation of flow-type landslides through their many phases. J. Fluid Mech. 779, 483–513. https://doi.org/10.1017/jfm.2015.383.

Dunatunga, S., Kamrin, K., 2017. Continuum modeling of projectile impact and penetration in dry granular media. J. Mech. Phys. Solids 100, 45–60. https://doi.org/10.1016/j.jmps.2016.12.002.

Engineering ToolBox, 2025. Friction coefficients for common materials. https://www.engineeringtoolbox.com/friction-coefficients-d_778.html.

Escobar, A., Baker, J., Guillard, F., Faug, T., Einav, I., 2025. Experimental confirmation of secondary flows within granular media. Nat. Commun. 16(1), 7446. https://doi.org/10.1038/s41467-025-62669-y.

Fang, J., Ji, W., Xue, T., Wang, Y., Zhao, J., Jiang, Y., Choi, C.E., 2026. A novel coupled MPM-SDEM framework for simulating non-spherical objects in flow-type landslide. Comput. Geotech. https://doi.org/10.1016/j.compgeo.2026.108163.

Fei, Y., Guo, Q., Wu, R., Huang, L., Gao, M., 2021. Revisiting integration in the material point method: a scheme for easier separation and less dissipation. ACM Trans. Graph. 40(4), 1–16. https://doi.org/10.1145/3450626.3459678.

Feng, L., 2024. Experimental research on the movement patterns of flat-shaped block in debris flows. Open Access Lib. J. 11(3), 1–14. https://doi.org/10.4236/oalib.1111344.

Feng, L., Song, D., 2025. Buried and displaced: moving characteristics of building fragments in debris flows. EGUsphere 2025, 1–27. https://doi.org/10.5194/egusphere-2025-5236.

Feng, Y.T., Owen, D.R.J., 2014. Discrete element modelling of large scale particle systems—I: Exact scaling laws. Comput. Part. Mech. 1, 159–168. https://doi.org/10.1007/s40571-014-0010-y

Fern, E.J., Soga, K., 2016. The role of constitutive models in MPM simulations of granular column collapses. Acta Geotechnica 11, 659–678. https://doi.org/10.1007/s11440-016-0436-x

Hübl, J., Suda, J., Proske, D., Kaitna, R., Scheidl, C., 2009. Debris flow impact estimation. In: Proceedings of the 11th international symposium on water management and hydraulic engineering. Vol. 1. University of Ss Cyril and Methodius, Faculty of Civil Engineering, Skopje, Macedonia, pp. 1–5. https://doi.org/10.5194/NHESS-2016-80.

Hungr, O., Evans, S.G., Bovis, M., Hutchinson, J., 2001. Review of the classification of landslides of the flow type. Environ. Eng. Geosci. 7(3), 231–238. https://doi.org/10.2113/gseegeosci.7.3.221.

Hürlimann, M., Rickenmann, D., Graf, C., 2003. Field and monitoring data of debris-flow events in the Swiss Alps. Can. Geotech. J. 40(1), 161–175. https://doi.org/10.1139/t02-087.

Indreiten, M., Svarstad, C., 2016. The Longyearbyen fatal avalanche accident 19th December 2015, Svalbard: lessons learned from avalanche rescue inside a settlement. In: Proceedings of the international snow science workshop, Breckenridge, Colorado. https://arc.lib.montana.edu/snow-science/objects/ISSW16_O16.01.pdf.

Iverson, R.M., 1997. The physics of debris flows. Rev. Geophys. 35(3), 245–296. https://doi.org/10.1029/97RG00426.

Iverson, R.M., Logan, M., LaHusen, R.G., Bunn, D.L., 2015. Scaling and design of landslide and debris-flow experiments. Geomorphology 244, 9–20. https://doi.org/10.1016/j.geomorph.2015.02.033.

Jiang, Y., Zhao, Y., Choi, C.E., Choo, J., 2022. Hybrid continuum–discrete simulation of granular impact dynamics. Acta Geotech. 17, 5597–5612. https://doi.org/10.1007/s11440-022-01598-2

Jiang, Y., Li, M., Jiang, C., Alonso-Marroquin, F., 2020. A hybrid material-point spheropolygon-element method for solid and granular material interaction. Int. J. Numer. Methods Eng. 121, 3021–3047. https://doi.org/10.1002/nme.6345.

Kean, J.W., Staley, D.M., Lancaster, J.T., Rengers, F.K., Swanson, B.J., Coe, J.A., Lindsay, D.N., 2019. Inundation, flow dynamics, and damage in the 9 January 2018 Montecito debris-flow event, California, USA: opportunities and challenges for post-wildfire risk assessment. Geosphere 15(4), 1140–1163. https://doi.org/10.1130/GES02048.1.

Lagmay, A.M.A., Tengonciang, A.M.P., Rodolfo, R.S., Soria, J.L.A., Baliatan, E.G., Paguican, E.R., Uichanco, C.L., 2008. Science guides search and rescue after the 2006 Philippine landslide. Disasters 32(3), 416–433. https://doi.org/10.1111/j.1467-7717.2008.01047.x.

Legislative Council of Hong Kong SAR, 2008. Debris fan slope statistics. https://www.legco.gov.hk/yr07-08/english/panels/de_panel/papers/de_panel0909cb2-2720-1-e.pdf.

Liang, Z., Choi, C.E., Zhao, Y., Jiang, Y., Choo, J., 2023. Revealing the role of forests in the mobility of geophysical flows. Comput. Geotech. 155, 105194. https://doi.org/10.1016/j.compgeo.2022.105194.

Liu, B., Wang, W., Liu, Z., Ouyang, N., Mao, K., Zhou, F., 2024. Study on large deformation of soil–rock mixed slope based on GPU accelerated material point method. Sci. Rep. 14, 6983. https://doi.org/10.1038/s41598-024-57362-x.

Liu, C., Sun, Q., Zhou, G.G., 2018. Coupling of material point method and discrete element method for flow-type landslides impacting simulations. Int. J. Numer. Methods Eng. 115, 172–188. https://doi.org/10.1002/nme.5800.

Liu, L., Ji, S., 2018. Ice load on floating structure simulated with dilated polyhedral discrete element method in broken ice field. Appl. Ocean Res. 75, 53–65. https://doi.org/10.1016/j.apor.2018.02.022.

Liu, R., Wang, F., Wang, J., Chen, X., Qiu, H., Lou, C., 2025. Experimental study on the movement of boulders in debris flow: influence of boulder size and initial orientation. Sustainability 17(1), 179. https://doi.org/10.3390/su17010179.

Luo, H., Zhang, L., He, J., Chen, H., 2019. Burial of structures in flow-type landslides. Eng. Geol. 261, 105278. https://doi.org/10.1007/s10346-019-01164-0.

Luo, H.Y., Zhang, L.M., He, J., Yin, K.S., 2022. Reliability-based formulation of building vulnerability to debris flow impacts. Can. Geotech. J. 59(1), 40–54. https://doi.org/10.1139/cgj-2020-0120.

Luo, R., Yu, Y., Ge, W., Sun, H., 2025. Hydrodynamic conditions governing the initiation of buried particles in dilute debris flows. Powder Technol. 121575. https://doi.org/10.1016/j.powtec.2025.121575.

Mani, P., Allen, S., Evans, S.G., Kargel, J.S., Mergili, M., Petrakov, D., Stoffel, M., 2023. Geomorphic process chains in high-mountain regions—a review and classification approach for natural hazards assessment. Rev. Geophys. 61(4). https://doi.org/10.1029/2022RG000791.

Mayer, F.T., Fringer, O.B., 2017. An unambiguous definition of the Froude number for lee waves in the deep ocean. J. Fluid Mech. 831, R3. https://doi.org/10.1017/jfm.2017.701.

Ng, C.W.W., Majeed, U., Choi, C.E., De Silva, W.A.R.K., 2021. New impact equation using barrier Froude number for the design of dual rigid barriers against debris flows. Landslides 18(6), 2309–2321. https://doi.org/10.1007/s10346-021-01631-7.

Prieto, J.A., et al., 2018. Development of structural debris flow fragility curves using momentum flux rate as a hazard parameter. Eng. Geol. 239, 144–157. https://doi.org/10.1016/j.enggeo.2018.03.014

Ren, S., Zhang, P., Galindo-Torres, S.A., 2022. A coupled discrete element material point method for fluid–solid–particle interactions with large deformations. Comput. Methods Appl. Mech. Eng. 395, 115023. https://doi.org/10.1016/j.cma.2022.115023.

Ren, S., Liu, Z., Trujillo-Vela, M.G., Galindo-Torres, S.A., Tian, X., Zhang, P., 2025. Simulation of solitary wave generation and wave-structure interactions using an MPM-SDEM coupling scheme. Ocean Eng. 340, 122195. https://doi.org/10.1016/j.oceaneng.2025.122195.

Salcedo, D. (2000). The December 1999 Catastrophic Debris Flows at Vargas State and Caracas, Venezuela, Characteristics and Lessons Learned. Proceedings of the XVI Seminario Sociedad, Venezolana de Geotecnia, 28-175.

Salciarini, D., Tamagnini, C., Conversini, P., 2010. Discrete element modeling of debris-avalanche impact on earthfill barriers. Phys. Chem. Earth 35, 172–181. https://doi.org/10.1016/j.pce.2009.05.002.

Schuster, R.L., 2006. Interaction of dams and landslides: case studies and mitigation. Reston, Virginia: US Geological Survey. https://doi.org/10.3133/pp1723.

Sovilla, B., Sonatore, I., Bühler, Y., Margreth, S., 2012. Wet-snow avalanche interaction with a deflecting dam: field observations and numerical simulations in a case study. Nat. Hazards Earth Syst. Sci. 12(5), 1407–1423. https://doi.org/10.5194/nhess-12-1407-2012.

Stomakhin, A., Schroeder, C., Chai, L., Teran, J., Selle, A., 2013. A material point method for snow simulation. ACM Trans. Graph. 32(4), 1–10. https://doi.org/10.1145/2461912.2461948

Sun, M., Li, J., Zhang, H., Chi, R., Pang, B., Cao, W., Xiao, J., 2024. Effect of relative density and grain size on the internal flow field during the ballistic penetration of sand. Int. J. Impact Eng. 185, 104859. https://doi.org/10.1016/j.ijimpeng.2023.104859.

Thouret, J.C., Antoine, S., Magill, C., Ollier, C., 2020. Lahars and debris flows: characteristics and impacts. Earth-Sci. Rev. 201, 103003. https://doi.org/10.1016/j.earscirev.2019.103003.

Trujillo-Vela, M.G., Galindo-Torres, S.A., Zhang, X., Ramos-Cañón, A.M., Escobar-Vargas, J.A., 2020. Smooth particle hydrodynamics and discrete element method coupling scheme for the simulation of debris flows. Comput. Geotech. 125, 103669. https://doi.org/10.1016/j.compgeo.2020.103669.

Yu, C., Leung, A.K., Zhu, J., Zhang, Y., Kootahi, K., Kumar, H., 2025. Successive boulder impacts on the soil-embedded baffle: an experimental study. Can. Geotech. J. (in press). https://doi.org/10.1139/cgj-2024-0787.

Zainali, A., Weiss, R., 2015. Boulder dislodgement and transport by solitary waves: insights from three - dimensional numerical simulations. Geophys. Res. Lett. 42(11), 4490–4497. https://doi.org/10.1002/2015GL063712.

Zhao, J., Zhao, S., Luding, S., 2023. The role of particle shape in computational modelling of granular matter. Nat. Rev. Phys. 5, 505–525. https://doi.org/10.1038/s42254-023-00613-7.

Zhao, W., Wang, R., Liu, X., Ju, N., & Xie, M. (2020). Field survey of a catastrophic high-speed long-runout landslide in Jichang Town, Shuicheng County, Guizhou, China, on July 23, 2019. Landslides, 17(6), 1415-1427. https://doi.org/10.1007/s10346-020-01380-z

Zhao, Y., Choo, J., Jiang, Y., Li, M., Jiang, C., Soga, K., 2022. A barrier method for frictional contact on embedded interfaces. Comput. Methods Appl. Mech. Eng. 393, 114820. https://doi.org/10.1016/j.cma.2022.114820.

Appendix A: Calibration of MPM-SDEM solver

A dedicated flume experiment was designed to validate the MPM-SDEM solver in Section 2.1.

The experimental setup is shown in Figure 2. And the flume is inclined at 10°, with an initial granular column, whose length is 0.3 m, width is 0.2 m, and height (H_i) is 0.2 m, formed by glass beads (particle diameter 0.002 m, bulk density 1600 kg/m³). A copper cube (side length 0.02 m, density 8900 kg/m³) was positioned 0.21 m (L_0) downstream of the granular column, with a measured block-flume basal friction coefficient of 0.67, as a constant. The granular mass was released by removing the gate, and the entire process was recorded at 60 FPS using a bottom-view high-speed camera through a transparent acrylic wall.

The corresponding MPM-SDEM simulation adopted identical geometry and material parameters (summarised in Table 2). The granular flow was modeled with MPM, using 96000 material points on a background grid of 0.01 m cubic cells (8 material points per grid). The copper block and flume bed were modeled with SDEM. Key contact parameters are shown in Table 2.

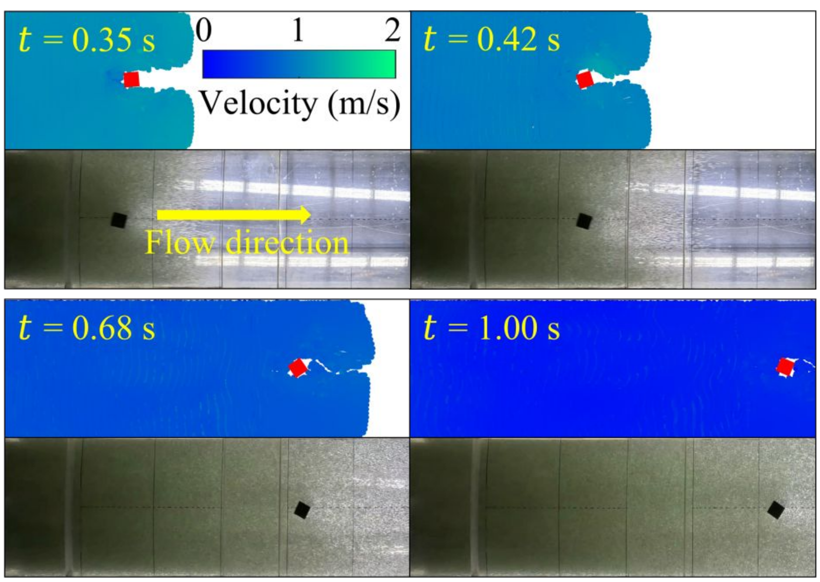

Figure A.1. Comparison of flow kinematics between measured and computed results

The calibration result is shown in Figure A.1. The computed flow kinematics faithfully reproduced the experimental impact sequence, including flow diversion around the block, subsequent sliding, and observable rotation of the cube. This independent flume benchmark demonstrates that the proposed MPM-SDEM framework accurately captures contact detection, and flow-block interaction at the MPM-SDEM interface, providing robust validation.

Appendix B: Robustness of the numerical results

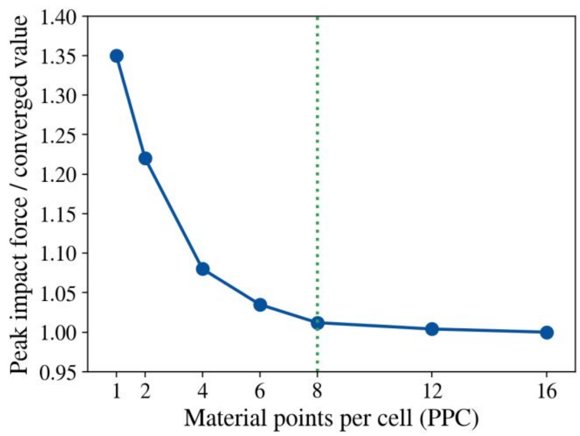

Figure B.1. Variation of the normalised peak impact force with the number of material points per cell (PPC) at fixed background-mesh size (10 mm). The force is normalised by the fine-PPC plateau (when PPC = 16).

The peak force decreases rapidly at low PPC and then approaches a near-constant value once a sufficient number of integration points is provided; beyond a practical threshold of about 6 MPs per cell, further enrichment yields only marginal change while computational cost continues to rise (Fern and Soga, 2016; Ceccato et al., 2024). The dotted vertical line marks the discretisation adopted in this study (PPC = 8), which lies in the near-converged regime. Similarly, the open-source MPM practice commonly recommends at least eight particles per cell (Blatny et al., 2025).

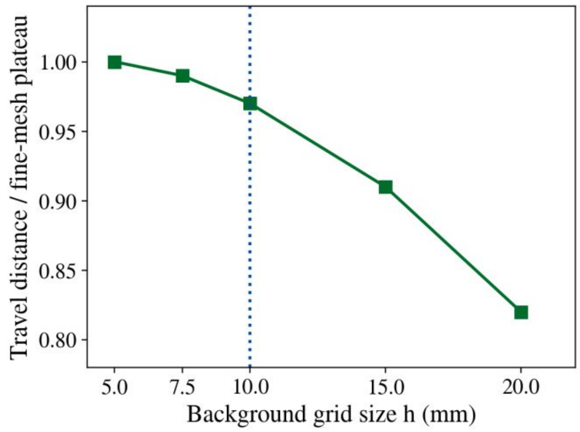

Figure B.2. Variation of the normalised block travel distance with background grid size h at fixed PPC. Travel distance is normalised by the fine-mesh plateau (h = 5 mm).

Coarsening the mesh under-resolves free-surface kinematics and contact transfer and can shift global runout-related metrics, whereas progressive refinement drives the solution toward a plateau with diminishing returns. Relative to h = 5 mm, the deviation at h = 10 mm is only about 3% (well below 5%), while the relative computational cost is substantially lower than that of the 5 mm discretisation. The dotted vertical line marks the grid size adopted in this study (h = 10 mm), chosen to balance numerical accuracy and computational performance for the large parametric matrix.